


Analysis and optimization of the demagnetization performance of permanent magnets of the hybrid excitation starter generator

JIN BIN XU  

*Automotive Engineering College, Zibo Vocational Institute
No. 506, Lian Tong Road, Zhoucun District, Zibo, Shandong Province, China
e-mail:  bin5613@163.com*

(Received: 03.05.2025, revised: 25.08.2025)

Abstract: The hybrid excitation starter generator (HESG) of range-extended electric vehicles is at risk of permanent magnet (PM) demagnetization under overload conditions. Therefore, this paper analyzes the operating process of PMs and the impact of armature reaction fields on PM operating points and demagnetization under various operating conditions. The variation patterns of average flux density operating points and minimum flux density values in the HESG under different load conditions are derived. The demagnetization points of each PM and their contributing factors are determined. Furthermore, the parameters of the magnetic isolation air gap between the PMs are optimized while considering leakage flux and demagnetization at the ends of the PMs. The simulation analysis and prototype test results show that a reasonable design and optimization of the ends of PMs can effectively enhance the demagnetization resistance of PMs and improve the output performance of HESG.

Key words: demagnetization performance, hybrid excitation starter generator, operating points of permanent magnets, optimization of parameters, range-extended electric vehicle

1. Introduction

Under generator mode conditions, the engine in the range extender (RE) of a range-extended electric vehicle (REEV) drives the generator to produce electricity, supplying power to the drive motor and the power battery. This effectively extends the driving range of the REEV, enabling it to deliver both eco-friendly performance and long-distance capability [1–4]. The integrated starter generator is one of the core components of the RE, requiring high efficiency,



© 2025. The Author(s). This is an open-access article distributed under the terms of the Creative Commons Attribution-NonCommercial-NoDerivatives License (CC BY-NC-ND 4.0, <https://creativecommons.org/licenses/by-nc-nd/4.0/>), which permits use, distribution, and reproduction in any medium, provided that the Article is properly cited, the use is non-commercial, and no modifications or adaptations are made.

fast response, and exceptional reliability [5]. This paper proposes a new hybrid excitation starter generator (HESG), which utilizes combined permanent magnets (PMs) and electromagnetic coils to generate a magnetic field together. Compared to a permanent magnet starter generator (PMSG), it offers adjustable main magnetic flux and superior voltage stabilization performance. Compared to an electrically excited starter generator, it reduces excitation power, leading to lower excitation losses and higher efficiency [6–8]. The demagnetization of PMs in HESG is a critical research subject. Irreversible demagnetization reduces the output performance of the generator and seriously affects its service life [9–11].

Currently, many scholars have researched the demagnetization characteristics of PMs and ways to improve their demagnetization resistance. Reference [12] used the conformal transformation method to derive the analytical model of the magnetic field under load condition of a surface mounted permanent magnet synchronous motor (PMSM), to analyze its influence on the internal magnetic induction strength of the PMs, and to determine the operating points of the PMs. However, the model did not reflect the change rule of the magnetic characteristic parameters of the PMs. Reference [13] proposed an algorithm and software based on discrete model equations to study the laws of PMs' partial demagnetization and the influence of operating temperature on the output characteristics for built-in U-type PMSM. However, an explicit model of the PMs' demagnetization mechanism is not given. Reference [14] analyzed the irreversible demagnetization of PMs of a built-in radial PMSM. It ensured the stability of the PMs in terms of demagnetization by determining the optimal parameters. Still, the method is mainly based on the eddy-current loss of the PMs, and the equivalent magnetic circuit method is used for modeling and analyzing. The model accuracy needs to be improved. Reference [15] studied the built-in V-type PMSM multi-objective optimization analysis method, the PMs demagnetization rate, and the maximum operating temperature as the optimization and validation objectives of the electromagnetic optimization of the motor. However, it did not give a detailed demagnetization rate calculation method or a mechanism model. Reference [16] analyzed the influence of PMs' parameters of a hybrid PMSG composed of NdFeB and ferrite PMs on its electromagnetic performance. It optimized the PMs' parameters with irreversible demagnetization amounts of PMs and basic electromagnetic parameters as the optimization objectives. However, the demagnetization amounts of PMs in the paper took the demagnetization volume as the analytical index, and the accuracy of the study needs to be improved. Reference [17] used the analytical method to calculate the operating points of PMs and studied the operating points of PMs and the inflection points of the demagnetization curve of PMs at the maximum operating condition, the demagnetizing current of the starter generator. However, the model uses the specific permeability of the PMs at no-load conditions as the variable for the calculation of the operating points of PMs, and the analytical model is relatively simple. Reference [18] used the method of combining field and circuit to calculate the electromagnetic parameters of the PM magnetic field in different PM magnetizing directions. It used this to establish the calculation model of the operating points of PMs. However, the model is based on a simplified magnetic circuit model, and the accuracy needs to be improved. Reference [19] used the finite element method to analyze the influence of different d - q axis armature reaction currents and operating temperatures on the demagnetization performance of PMs in a built-in V-type PMSG, and put forward a method to improve the demagnetization resistance of PMSG. However, the reference only analyses the demagnetization mechanism based on the PMs' demagnetization curve and the PMs' density calculation method.

Comprehensive analysis shows that most of the scholars on the study of PM demagnetization performance mostly use the magnetic circuit method, the conformal transformation method and other numerical methods to obtain the magnetic field analytical model, analyze the operating magnetic density of PMs, and then study the influence of electromagnetic parameters, operating temperature and other PM demagnetization performance, study the optimization of demagnetization resistance through the electromagnetic design or study the influence of some demagnetization conditions on the output performance of the whole machine. The numerical analysis model based on the magnetic field distribution mainly reacts to the magnetic field distribution of the whole machine, and it is difficult to directly react to the magnetic properties of PMs. Moreover, the current research on the demagnetization of PMs is mostly aimed at a single form of PM pole structure, and it is difficult to apply the research methodology and conclusions to the combined pole structure. Therefore, this paper from the PMs operating points and demagnetization mechanism, based on the graphical method to study the different conditions of the PM work process model, and the use of the finite element method to analyze and verify the Combined Magnetic Poles rotor PM work of the magnetic density change rule and demagnetization resistance performance.

2. Topological structure of HESG

The new HESG proposed in this paper consists of a combined pole PM rotor axially juxtaposed with a brushless electro-excitation rotor. The structure is shown in Fig. 1.

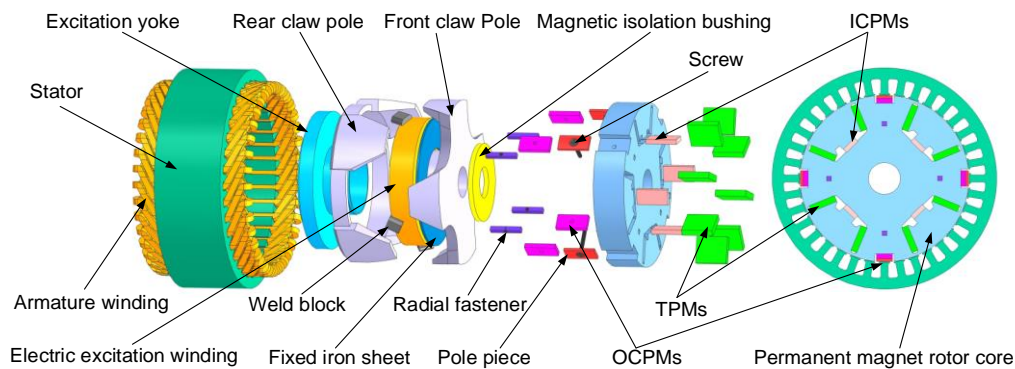


Fig. 1. Structure diagram of HESG

The permanent magnet part of the HESG adopts a combined pole structure combining built-in tangential permanent magnets (TPMs) and inner combined permanent magnets (ICPMs) as well as buried outer combined permanent magnets (OCPMs), and the electric excitation part adopts a cantilevered brushless claw pole structure. The main technical indexes and structural parameters of the HESG are shown in Table 1.

Table 1. Main technical indexes and structural parameters of the HESG

Parameter	Value	Parameter	Value
Rated power (W)	1 000	Axial length of stator (mm)	43
Rated speed (rpm)	4 000	Thickness of claw pole flange (mm)	8.5
Rated voltage (V)	84	Thickness of yoke inside claw pole (mm)	10
Outer diameter of stator (mm)	140	Axial length of permanent magnet rotor (mm)	20
Inner diameter of stator (mm)	106	Effective axial length of electrically excited rotor (mm)	20
Length of main air gap (mm)	0.4	Length of excitation yoke additional air gap (mm)	0.4
Inner diameter of rotor (mm)	26	Thickness of claw root (mm)	8
Length of TPMs (mm)	20	Thickness of claw tip (mm)	3
Width of TPMs (mm)	5	Thickness of excitation yoke (mm)	8.5
Length of ICPMs (mm)	10	Materials of PMs	N38H_120°
Width of ICPMs (mm)	3.5	Materials of stator core	DW310-35
Length of OCPMs (mm)	10	Materials of rotor core	DW310-35
Width of OCPMs (mm)	3.5	Materials of pole piece	Cast iron

3. Analysis of demagnetization mechanism and operating process of PMs

This paper analyzes the effect of armature reaction on the demagnetization performance of PMs by combining the demagnetization mechanism of PMs. The armature reaction magnetic field forms a circuit through the main air gap and the rotor core, changing the rotor magnetic kinetic potential waveform and producing the effects of magnetizing and weak magnetism. Armature reaction magnetic field where the magnetic circuit is not saturated, the armature reaction to the magnetic field of the magnetization and the weak magnetic effect are equal. Vice versa will make the magnetic circuit saturated and produce a magnetization or demagnetization of the PM, so that the PM's operating points and output performance change, PM's demagnetization curve, and the variation of PM's operating points are shown in Fig. 2.

From Fig. 2(a), the operating point of the PM is M_p under no load conditions. Under load conditions, there is an armature reaction magnetic field, which produces magnetization or weak magnetization on the magnetic field of the PM, and the operating point moves along the demagnetization curve to the left and right. From Fig. 2(b), the operating point of PM moves to the left along the demagnetization curve under the effect of weak magnetism, and when the weak magnetic field disappears, the operating point returns to M_p along the demagnetization curve to the right. From Fig. 2(c), when the weak magnetic field is larger, the PM will follow the demagnetization curve to reach a point p below the knee point k . When the weak magnetic field disappears, the PM will not be able to return to the original operating point along the demagnetization curve, but will follow the recurrent line lower than the demagnetization curve to

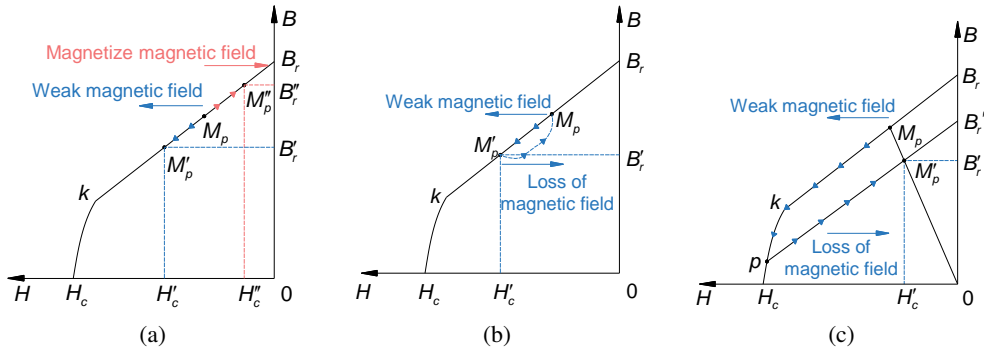


Fig. 2. PMs demagnetization curve and variation of PMs operating points: demagnetization curve (a); operating points variation under weak magnetic condition (b); operating points variation under demagnetization condition (c)

reach the new operating point M'_p . The magnetization of the PM at M'_p is even smaller, the PM produces permanent demagnetization, and its residual magnetization is reduced to B'_r . When the weak magnetic field increases again, the PM is demagnetized and reaches the new operating point until completely demagnetized. Therefore, in order to ensure the regular operation of the PMs, the effect of the armature reaction on the operating process of the PMs should be analyzed [20–22].

The operating process of the PMs under armature reaction can be analyzed graphically [23, 24]. In order to simplify the analysis, the PM is equivalent to the magnetic momentum in series with the internal magnetic permeability, and the outer magnetic circuit of the PM field is equivalent to the magnetic permeability in series with the magnetic momentum using Thevenin's theorem. The effect of the leakage flux of the outer magnetic circuit is expressed in terms of the leakage coefficient σ , and the magnetic energy supplied by the PM is expressed in terms of the magnetic potential F_m and the magnetic flux Φ_m [25, 26]. The operating process of the PM obtained by the graphical method under no load and load conditions is shown in Fig. 3.

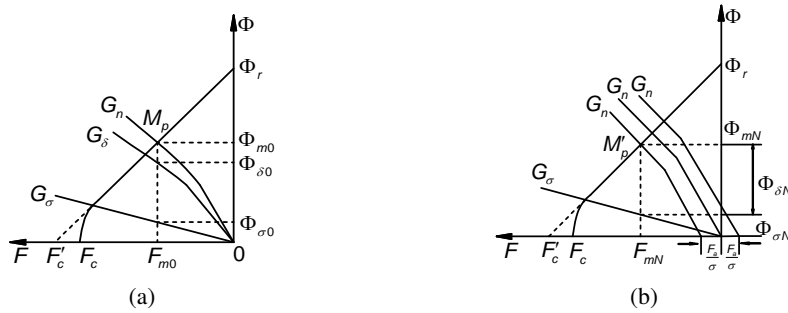


Fig. 3. Operating process of the PM under different operating conditions: operating process under no-load condition (a); operating process under load condition (b)

From Fig. 3, $\Phi_m = f(F_m)$ is the recoil line of the PM, and its intersection with the coordinate axis Φ_r is the residual magnetic flux of the PMs, and F_c is the coercive magnetic potential. $G_n = f(\Phi_m)$ is the change curve of the magnetic permeability and flux of the external magnetic

circuit, which is written as the synthesized magnetic guideline. The graphical method to solve the operating point of the PM is to find the intersection of the PM recoil line and the synthesized magnetic guide line. From Fig. 3(a), $G_\delta = f(\Phi_m)$ is the variation curve of the main air gap permeance versus the main magnetic flux. $G_\sigma = f(\Phi_m)$ is the variation curve of the leakage permeance versus the main magnetic flux. Add two curves along the longitudinal axis to obtain the synthesized permeance curve $G_n = f(\Phi_m)$, the intersection of this curve with the PM recovery curve M_p is the operating point under no load. Φ_{m0} and F_{m0} are the magnetic flux and magnetic kinetic potential supplied outward by the PM at this point, respectively, and the intersection of the vertical line through this point with the synthetic magnetic lead corresponds to the leakage flux $\Phi_{\sigma 0}$ and the main air gap flux $\Phi_{\delta 0}$. From Fig. 3(b). There is an armature magnetic motive force F_a or equivalent magnetic motive force F'_a in the external magnetic circuit under load, $F'_a = \frac{F_a}{\sigma}$. When the armature reacts to the magnetic field to increase the magnetism or weaken magnetism, the magnetic momentum acting on the synthetic magnetic guide of the external magnetic circuit is $F_m + F_a$ or $F_m - F'_a$, so the synthetic magnetic guide needs to be translated from the origin to the right or the left of $|F'_a|$. At this time, the intersection of the synthetic magnetic guide with the recoil line M'_p is the new operating point of the PM load condition, and the corresponding Φ_{mN} and F_{mN} are the magnetic flux and magnetic momentum provided by the PM to the outside at this time, and the intersection of the vertical line through this point with the synthetic magnetic guide is corresponds to the leakage flux $\Phi_{\sigma N}$, the main air gap flux $\Phi_{\delta N} = \Phi_{mN} - \Phi_{\sigma N}$.

The electromagnetic parameters of the operating points of PMs are usually calculated using the per-unit, the per-unit of each electromagnetic parameter is calculated as [27, 28]:

$$\begin{aligned} \varphi_m &= \frac{\Phi_m}{\Phi_r} = \frac{B_m}{B_r} = b_m, \\ f_m &= \frac{F_m}{F_r} = \frac{H_m}{H_r} = h_m, \\ f'_a &= \frac{F'_a}{F_c} = h'_a, \\ \lambda_\delta &= \frac{\Lambda_\delta}{\Lambda_0}, \end{aligned} \quad (1)$$

where: φ_m is the main magnetic flux supplied by the permanent magnetic field, b_m is the longitudinal coordinate of the operating point, B_m is the magnetic induction intensity of the PM, B_r is the remanent magnetization of the PM, f_m is the magnetic motive force provided by the PM, h_m is the horizontal coordinate of the operating point of the PM, f'_a is the armature magnetic motive force, h'_a is the armature reaction magnetic field parameter, and λ_δ is the main magnetic circuit permeance.

No-load condition armature magnetic motive force is zero. At this time, the demagnetization curve of PMs and the equivalent magnetic circuit calculation formula are:

$$\begin{cases} \varphi_{m0} = 1 - f_{m0} \\ \frac{\varphi_{m0}}{f_{m0}} = \lambda_\delta + \lambda_\sigma = \lambda_n \end{cases}, \quad (2)$$

where: φ_{m0} is the per-unit of the total magnetic flux provided by PMs, f_{m0} is the per-unit of the magnetic motive force provided by PMs, λ_σ is the per-unit of leakage permeance, and λ_n is the per-unit of external magnetic circuit permeance, $\lambda_\sigma = \frac{G_\sigma}{G_0}$, $\lambda_n = \frac{G_n}{G_0}$.

The no-load operating point (b_{m0}, h_{m0}) of PMs can be obtained by solving Eq. (2):

$$\begin{cases} \varphi_{m0} = \frac{\lambda_n}{\lambda_n + 1} = b_{m0} \\ f_{m0} = \frac{1}{\lambda_n + 1} = h_{m0} \end{cases} \quad (3)$$

The permanent magnetic field is changed by the armature reaction under load conditions, the operating point (b_{mN}, h_{mN}) of PMs is:

$$\begin{cases} \varphi_{mN} = \frac{\lambda_n (1 - f'_a)}{\lambda_n + 1} = b_{mN} \\ f_{mN} = \frac{1 + \lambda_n f'_a}{\lambda_n + 1} = h_{mN} \end{cases}, \quad (4)$$

where: φ_{mN} is the per-unit of the total magnetic flux of PMs and f_{mN} is the per-unit of the magnetic motive force provided by PMs.

The above $\Phi_m - F_m$ coordinate can be used to quickly find out the electromagnetic parameters, such as magnetic flux and magnetic potential, corresponding to the operating point according to the position of the operating point. However, it is more difficult to reflect the properties of the PMs. For this reason, the $\Phi_m - F_m$ coordinate is transformed into the magnetic flux density-magnetic field strength $(B_m - H_m)$ coordinate diagram of the PMs, the formula is:

$$\begin{cases} B_m = \frac{\Phi_m}{A_m} \\ H_m = \frac{F_m}{l} \end{cases}, \quad (5)$$

where: A_m is the cross-sectional area of the magnetic field of PMs, $A_m = a_m L_m$, a_m is the length of PMs, L_m is the axial length of PMs, l is the average length of the magnetic circuit.

The operating process of the PMs under load conditions in the $B_m - H_m$ coordinate is shown in Fig. 4.

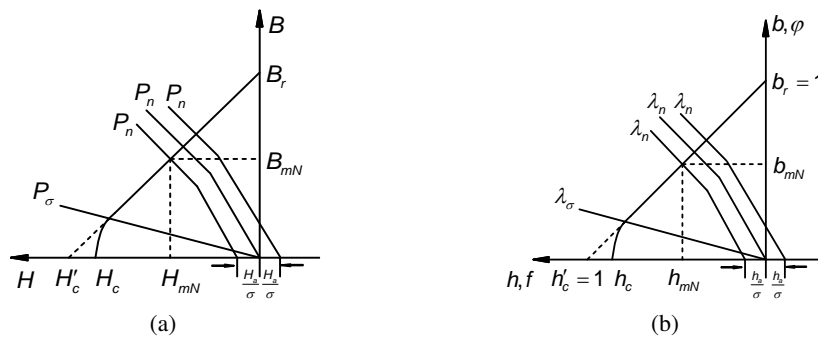


Fig. 4. Operating process of the PMs under load condition: work processes expressed in terms of parameters (a); work processes expressed in terms of the per-unit of parameters (b)

From Fig. 4(a), $B_m = f(H_m)$ is the demagnetization curve of the PM, $P_n = f(B_m)$ is the change curve of the flux density and magnetic field strength of the external magnetic circuit, B_{mN} and H_{mN} are the flux density and magnetic field strength at the operating point of the PM, and H_a is the magnetic field strength generated by the armature reaction magnetic field. When the armature reaction magnetic field plays the role of magnetization or weak magnetism, the curve $P_n = f(B_m)$ needs to be shifted to the right or the left from the origin $\frac{H_a}{\sigma}$. Figure 4(b) shows the operating process of the PMs expressed by the per-unit of each electromagnetic parameter under the $B_m - H_m$ coordinate, and the analysis process is the same as that in Fig. 4(a). From Fig. 4, when analyzing the operating point of the PMs, the flux density or magnetic field strength of the operating point can be compared with that of the knee point [29,30].

4. Analysis of PM demagnetization performance and optimization of demagnetization resistance performance

4.1. Analysis of PM demagnetization performance

Based on the operating process of PMs, the finite element method is used to model and simulate the HESG for verification. The finite element model is based on the mathematical model of magnetic field analysis obtained from Maxwell's equations [31].

$$\begin{aligned} \int_t H \cdot dl &= \int_S J \cdot dS + \frac{\partial}{\partial t} \int_S D \cdot dS, \\ \int_t E \cdot dl &= -\frac{\partial}{\partial t} \int_S B \cdot dS, \\ \int_S B \cdot dS &= 0, \\ \int_S D \cdot dS &= \int_V \rho \cdot dV, \end{aligned} \quad (6)$$

where the relationship between the field quantities is: $D = \varepsilon E$, $B = \mu H$, $J = \sigma E$.

The fluctuation equation of the electromagnetic field is obtained from the fluctuation equation with the vector magnetic potential A as a function of the field variable and the fluctuation equation with the scalar potential function ϕ as a function of the field variable as:

$$\begin{cases} \nabla^2 A - \mu\varepsilon \frac{\partial^2 A}{\partial t^2} = -\mu J \\ \nabla^2 \phi - \mu\varepsilon \frac{\partial^2 \phi}{\partial t^2} = -\frac{\rho}{\varepsilon} \end{cases}. \quad (7)$$

The numerical finite element equation for transient operating conditions is as follows [32]:

$$\nabla \times v (\nabla \times A) = J_0 \times (v\mu_0 M_r), \quad (8)$$

where v and J_0 are the magnetoresistance and excitation current density, respectively. μ_0 and M_r are the permeability and magnetisation of free space, respectively.

The PMs in this paper are N38H_120°, the coercivity is 946.3 kA/m, the remanent magnetization is 1.109 T, and the demagnetization inflection points flux density is 0.402 T. To simplify the analysis, ignores the effect of temperature on the operating points of PMs and sets a constant operating temperature. The average magnetically dense operating points of PMs under different operating conditions of the HESG are calculated as in Table 2.

Table 2. Average magnetic density operating points of PMs under different operating conditions

Operating condition	TPMs	ICPMs	OCPMs
No load condition	0.820	0.759	0.998
Half load condition	0.804	0.737	0.994
Rated load condition	0.782	0.708	0.987
50% overload condition	0.761	0.681	0.979

Table 2 shows that the magnetic density operating points of the OCPMs are 0.998, which is bigger than the other two PMs. This is due to both TPMs and the ICPMs having a part of the magnetic circuit through the OCPMs, which increases the magnetic density of the OCPMs. As the load power increases, the effect of the HESG armature reaction on the PMs increases, and the operating point decreases. Under rated load condition, the magnet density operating point of TPMs is reduced to 0.782, and under 50% overload condition, it is reduced to 0.761. The ICPMs magnetic density operating point decreases to 0.708 under the rated load condition, and decreases to 0.681 under 50% overload.

To improve the utilization of the PM, it is desired that it can produce maximum magnetic energy in the main magnetic field. At this time, the operating point is called the optimum operating point. The magnetic energy provided by the PM is calculated as [33]:

$$\frac{1}{2} \Phi_D F_D = \frac{1}{2} (BH) V_{pm}, \quad (9)$$

where: Φ_D is the magnetic flux supplied by PMs, F_D is the magnetic motive force provided by PMs, and (BH) is the magnetic energy product of PMs.

From the above formula, the larger the magnetic energy product of PMs, the smaller the volume used. From the operating process of PMs, the operating points at the maximum magnetic energy product of PMs should be at the midpoint of the curve, but the magnetic energy generated by PMs can't be completely converted into the effective magnetic energy of the main magnetic field and there is leakage flux in the magnetic field, the optimum operating points of PMs is larger than the midpoint of the curve. Also, other properties of the motor need to be considered in the design of PMs. Therefore, the operating point is taken in the range of $b_{m0} \approx 0.6 \sim 0.85$. In this paper, the operating points of TPMs and ICPMs under no load conditions are 0.820 and 0.759, respectively, which are within the optimal operating point design of PMs. The OCPMs are located outside of the magnetic pole. The magnetic field strength is large, making it difficult to reduce its operating magnetism, so the operating point of OCPMs is not considered.

Then, the minimum magnetic density point of each PM under different operating conditions of the generator is analyzed to analyze the effect of armature reaction on the demagnetization of the PMs. Using finite element software to calculate the minimum magnetic density of the PMs under different operating conditions of the HESG, as shown in Table 3.

Table 3. Minimum magnetic density of PMs under different operating conditions

Operating condition	TPMs	ICPMs	OCPMs
No load condition	0.555	0.590	1.091
Half load condition	0.489	0.525	1.006
Rated load condition	0.410	0.443	0.898
50% overload condition	0.348	0.374	0.866

Table 3 shows that the minimum magnetic density of TPMs and the ICPMs under rated load conditions are respectively 0.410 T and 0.443 T, the PMs are not demagnetized. However, when the HESG is running overloaded by 50%, the minimum magnet density of these two types of PMs is, respectively, 0.348 T and 0.374 T, which is smaller than the demagnetization inflection points, the demagnetization at the points of minimum magnetization density occurs. When under 50% overload condition, the flux density of TPMs and the ICPMs is shown in Fig. 5.

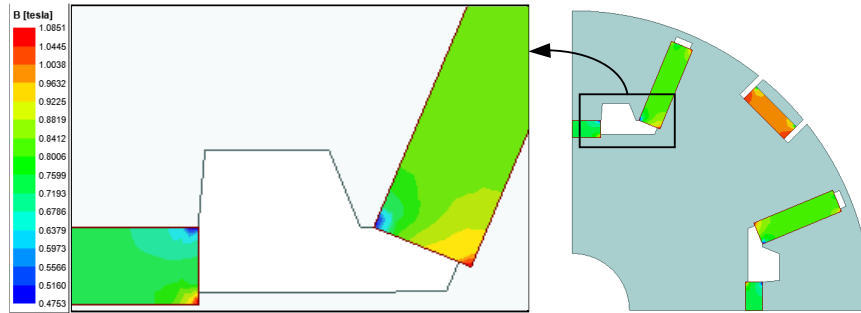


Fig. 5. Magnetic flux density of two PMs at the minimum magnetic density point

From Fig. 5, the minimum magnetic density points of both PMs are distributed on both sides of the magnetic isolation air gap. Since the large internal resistance of the air gap, the armature's reactive magnetic field is mainly distributed on both sides of the air gap, thus affecting the two PMs. The two PMs only have a small portion of local demagnetization near the endpoints, the flux density in most of the area is greater than the inflection points of the PMs.

The demagnetization rate k_{dc} of PMs is the ratio of the remanent magnetization recovered by the PMs after the weak magnetic field has receded to the remanent magnetization of the PMs, and is calculated by the following formula [34, 35]:

$$k_{dc} = \frac{B_{r1}}{B_r}, \quad (10)$$

where B_{r1} is the remanent magnetization of the PM after recovery.

When the PMs are not demagnetized, the k_{dc} is 1, and it is 0 when the PMs are completely demagnetized. Finite element simulation and PM demagnetization rate calculation are carried out for the 50% overload condition of the HESG. To improve the accuracy of the simulation results, transient simulation is used to obtain the change curve of the PM demagnetization rate with time, and the average value of the PM demagnetization rate over some time after it stabilizes is taken for analysis. The variation curves of demagnetization rate with time at the minimum magnetic density point of the two PMs are shown in Fig. 6.

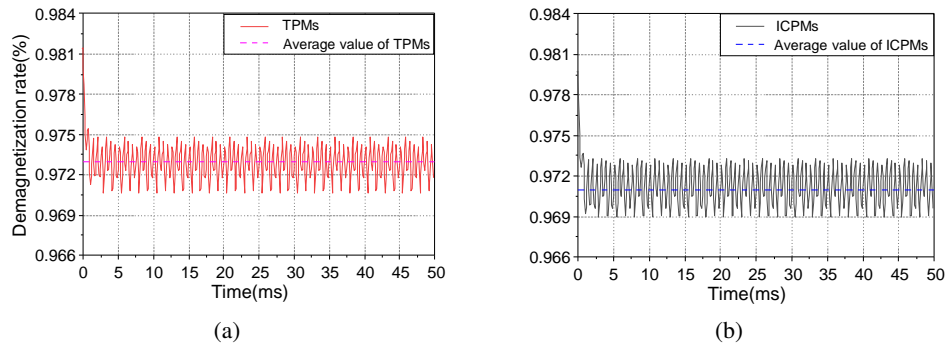


Fig. 6. Demagnetization rate with time at the minimum magnetic density point of the two PMs: demagnetization rate of TPMs (a); demagnetization rate of ICPMs (b)

From Fig. 6, after commencing generator operation, the demagnetization rate at the minimum magnetization point of the two PMs decreases initially, then exhibits a periodic change, and remains stable. The average demagnetization rates at the minimum magnetic density points of TPMs and ICPMs are 0.973 and 0.971, respectively. The demagnetization amounts of the two PMs are minimal. Set the HESG to 50% overload condition, formulate the demagnetization rate of the PMs in the finite element software's field solver, and include the calculation of the demagnetization rate of the PMs in the simulation setup to obtain the demagnetization rates of the two PMs during the stabilization of the HESG under 50% overload, as shown in Fig. 7.

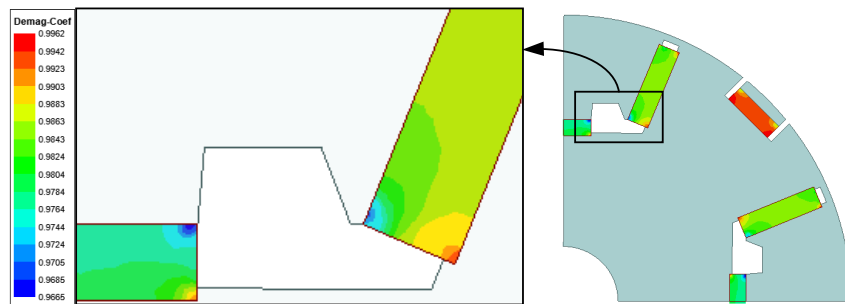


Fig. 7. Demagnetization rate of two PMs at the point of minimum magnetic density

From Fig. 7, most of the demagnetization rate is above 0.98, the demagnetization rate at the operating point of the minimum magnetic density is about 0.97, but the area of this region is tiny, which has less influence on the operating performance of PMs. The demagnetization points of

PMs are mainly distributed on both sides of the connecting magnetic isolation air gap, the reason is that the air gap has a larger magnetoresistance, and the magnetic field of the d-axis armature reaction will form a circuit on both sides of it. Therefore, the reasonable design of the structure of the connecting air gap can weaken the influence of the armature reaction on the demagnetisation performance of the PMs.

4.2. Optimization of demagnetization resistance performance

1) Trapezoidal bottom angle of the connecting magnetic isolation air gap

When the height of the air gap is 3 mm, the influence law of the bottom angles of the air gap on the minimum magnet density of the ICPMs is shown in Fig. 8.

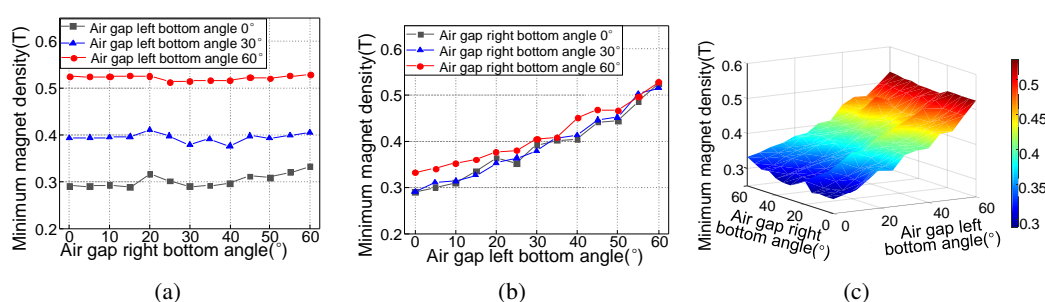


Fig. 8. Influence law of air gap bottom angles on the minimum magnet density of the ICPMs: variation of right bottom angle at different left bottom angle (a); variation of left bottom angle at different right bottom angle (b); left and right bottom angles change simultaneously (c)

From Fig. 8(a), when the left bottom angle of the air gap is constant, the minimum magnet density of the ICPMs increases slowly with the right bottom angle. When the left bottom angle increases from 0° to 60°, the minimum magnet density of the ICPMs increases from 0.3 T to 0.52 T, which gradually exceeds the demagnetization inflection points of PMs, as shown in Fig. 8(b). When the left bottom angle is more than 30°, the minimum magnetic density of the ICPMs is more than 0.4 T. At this time, the ICPMs do not demagnetize when the HESG is under 50% overload condition. From Fig. 8(c), the minimum magnet density of the ICPMs has a smaller growth trend when the right bottom angle increases, and the minimum magnet density of the ICPMs almost increases linearly with the increase of the left bottom angle. The ICPMs can be guaranteed not to demagnetize under this condition when the left bottom angle is varied in the range of 30° to 60°.

When the height of the air gap is 3 mm, the influence of the bottom angles of the air gap on the minimum magnet density of the TPMs is shown in Fig. 9.

From Fig. 9(a), the minimum magnet density of the TPMs shows a tendency of increasing, decreasing, and then increasing with the increase of the right bottom angle, reaching a maximum value around 20° and a minimum value around 25°. From Fig. 9(b), the minimum magnet density of TPMs increases slowly with the increase of the left bottom angle. From Fig. 9(c), the variation of the right bottom angle has a greater effect on the minimum magnet density of PMs. When the right bottom angle is around 20°, the maximum of the minimum magnet density of TPMs is 0.35 T, which is still smaller than the demagnetization inflection points of PMs. When the HESG is under 50% overload condition, the height can't prevent the TPMs not demagnetizing. So, the air

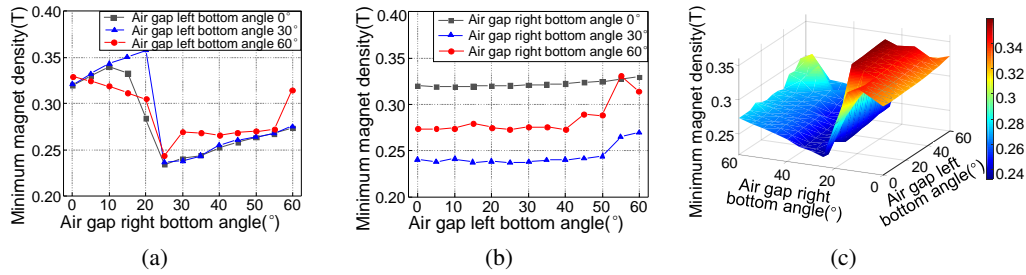


Fig. 9. Influence law of bottom angles of air gap on minimum magnet density of the TPMs: variation of right bottom angle at different left bottom angle (a); variation of left bottom angle at different right bottom angle (b); left and right bottom angles change simultaneously (c)

gap height is changed to study the effect of the size of the right bottom angle on the operating points of the TPMs magnetic density, the minimum magnet density variation surface of TPMs is shown in Fig. 10 when the left bottom angle of the air gap is from 30° to 60° and the heights of the air gap are 1.5 mm, 2 mm and 2.5 mm, respectively.

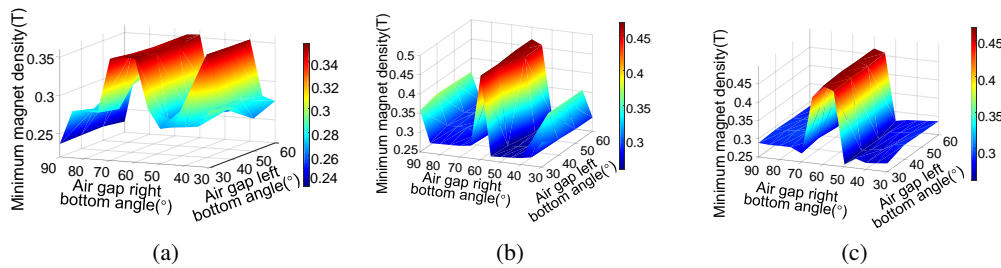


Fig. 10. Variation law of the minimum magnet density of TPMs with different air gap heights: height is 2.5 mm (a); height is 2 mm (b); height is 1.5 mm (c)

From Fig. 10(a), when the height is 2.5 mm, the minimum magnet density of TPMs shows a fluctuating trend with the increase of the right bottom angle, and reaches a maximum value when the right bottom angle is 35°, 50° and 70°. The maximum of the minimum magnet density of TPMs is 0.35 T, which is still smaller than the demagnetization inflection points. When the height is 2 mm, the minimum magnet density of TPMs shows an increasing and then decreasing trend with the increase of right bottom angle, and reaches a maximum value 0.47 T when the right bottom angle is in the range of 55° to 65°, the PMs do not demagnetize. When the height is 1.5 mm, the minimum magnet density of TPMs shows a tendency of increasing and then decreasing with the increase of the right bottom angle, and reaches the maximum value in the range of 35° to 50°, with the maximum value of 0.47 T. The PMs are not demagnetized.

2) Trapezoidal height of the connecting magnetic isolation air gap

When the left bottom angles are respectively 50°, 60°, and the air gap heights are respectively 1.5 mm, 2 mm, and 2.5 mm, the variation curves of the minimum magnet density of TPMs with the right bottom angle are shown in Fig. 11.

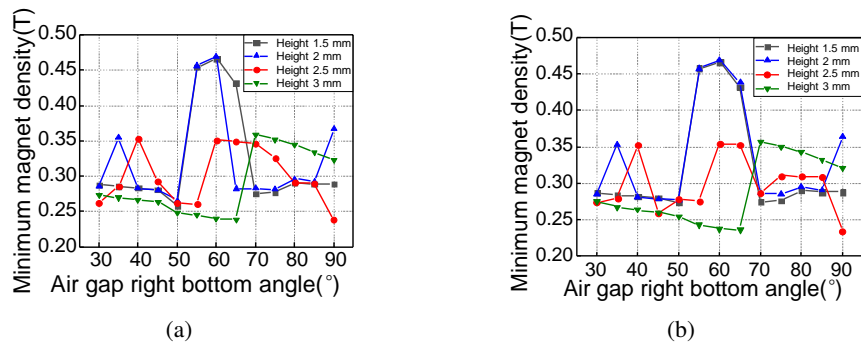


Fig. 11. Variation law of minimum magnetic density of TPMs with different air gap left bottom angles and heights: left bottom angle is 50° (a); left bottom angle is 60° (b)

From Fig. 11, as the height of the air gap increases, the minimum magnet density of TPMs increases. The minimum magnet density of TPMs respectively reaches the maximum value at different right bottom angles for different heights. When the height is less than 2 mm and the right bottom angle is 60° , it reaches the maximum value 0.47 T, which can ensure that the PMs are not demagnetized. Different left bottom angles affect the distribution interval of the minimum magnet density maximum of TPMs, which is from 55° to 60° when the left bottom angle is 50° , and from 50° to 65° when the left side bottom angle is 60° . As the analysis of the magnetic leakage, the larger the left bottom angle and height of the air gap, the smaller the leakage coefficient, and the larger the main magnetic flux can be obtained from the magnetic field of PMs. After a comprehensive analysis, a right bottom angle of 60° and a height of 2 mm are suitable for the TPMs.

Then, the effect of air gap height on the ICPMs was analyzed. The variation surface of the minimum magnet density of the ICPMs is shown in Fig. 12 when the heights are 1.5 mm, 2 mm, and 2.5 mm, respectively.

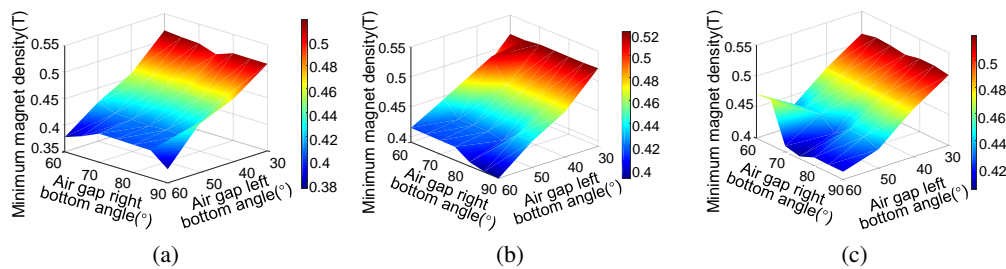


Fig. 12. Variation law of the minimum magnetic density of the ICPMs with different air gap heights: height is 2.5 mm (a); height is 2 mm (b); height is 1.5 mm (c)

From Fig. 12, when the height of the air gap is different, the minimum magnetic density of the ICPMs decreases with the increase of the left bottom angle, and increases with the decrease of the height. The right bottom angle has less effect on the minimum magnet density of the ICPMs. The variation curves of different air gap heights on the minimum magnet density of the ICPMs are shown in Fig. 13 when taking the right bottom angles of 50° and 60° .

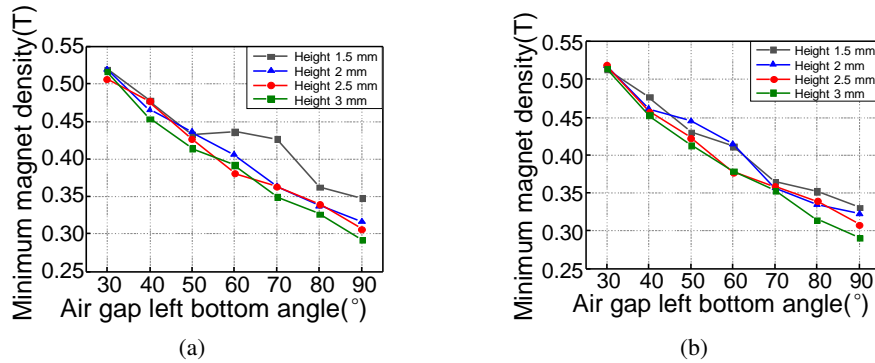


Fig. 13. Variation law of minimum magnetic density of the ICPMs with different air gap right bottom angles and heights: right bottom angle is 50° (a); right bottom angle is 60° (b)

From Fig. 13, when the height is 2 mm and the left bottom angle is less than 60°, the minimum magnet density of the ICPMs is more than 0.4 T. As the analysis of the magnetic leakage, with the left bottom angle decreases, the leakage flux increases. After comprehensive consideration, the selection is the left bottom angle of 50°. At this time, the minimum magnetic density of the TPMs and the ICPMs is 0.47 T and 0.45 T. This air gap ensures that under 50% overload conditions, the two types of PMs will not demagnetize. When the height of the air gap is 2 mm, the change in surface rule of the operating point of TPMs and the ICPMs is shown in Fig. 14 when the left and right bottom angles are changed at the same time.

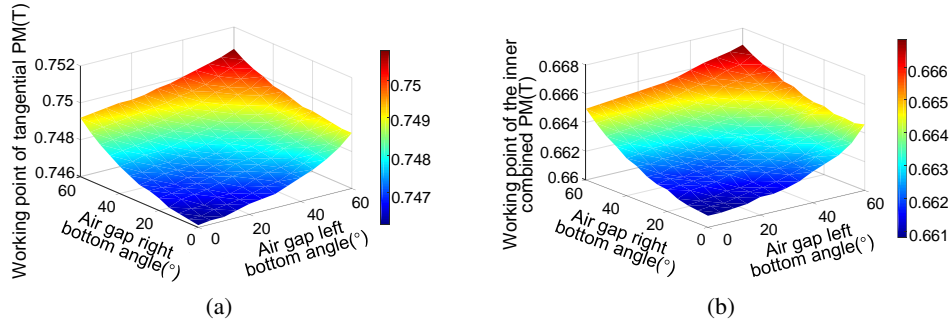


Fig. 14. Influence of the different left and right bottom angles on the operating point of two PMs: operating point of TPMs (a); operating point of the ICPMs (b)

From Fig. 14, with the increasing left and right bottom angles, the magnetic density operating point of the TPMs and the ICPMs increases. When the left and right bottom angles are 50° and 60°, the magnetic density operating points of TPMs and the ICPMs are respectively 0.745 T and 0.658 T, which are within the optimum range of the operating point. When the height is 2 mm and the left and right bottom angles are respectively 50° and 60°, the leakage flux is 2.383×10^{-5} Wb, the flux leakage coefficient of the permanent magnetic field is 1.212, which is only increased by 0.001 compared with the original design value, the permanent magnetic field has smaller flux leakage coefficient with this design parameter.

5. Prototyping and testing

A HESG prototype with a rated power of 1 kW and a rated voltage of 84 V was fabricated based on the best parameters optimised for the PMs demagnetization resistance, as shown in Fig. 15.

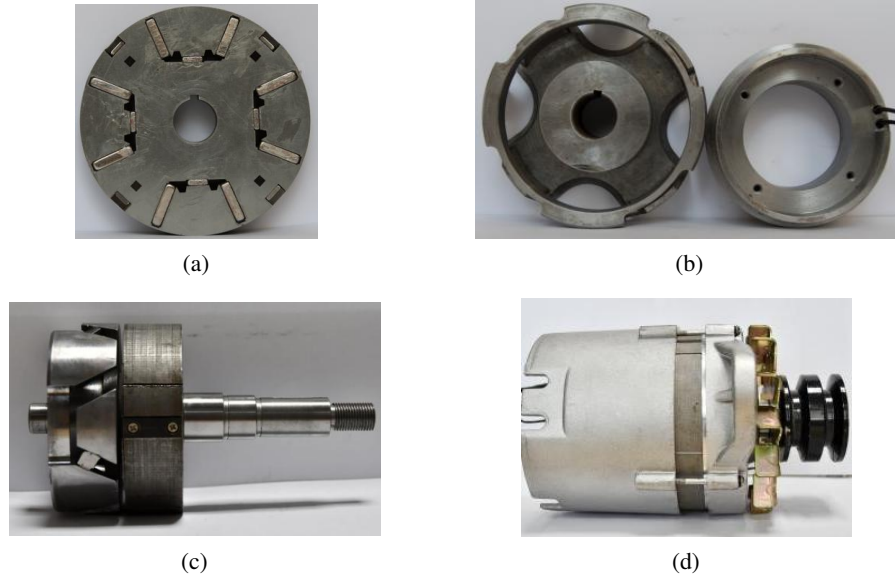


Fig. 15. Pictures of HESG prototype: permanent magnet rotor (a); electric excitation rotor (b); parallel combined rotor (c); overall prototype (d)

To verify the output performance of the HESG, a test platform is built and prototype tests are carried out, as shown in Fig. 16.

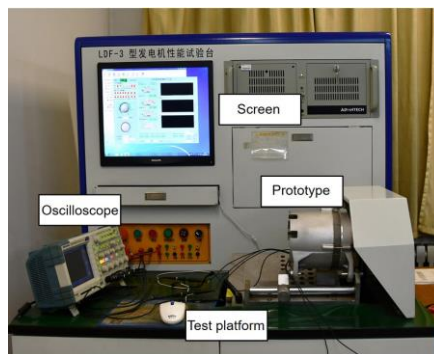


Fig. 16. HESG prototype test platform

Sets HESG speed to 4 000 rpm and tests the no load induced electromotive force curve as shown in Fig. 17(a). Still sets this speed, fixes the exciting current 0.8 A, changes the load, and tests output voltage, the external characteristic curve of the HESG is shown in Fig. 17(b). Still sets this speed, changes load current, and realizes rated voltage output by adjusting exciting current, the field current regulation characteristic curve is shown in Fig. 17(c).

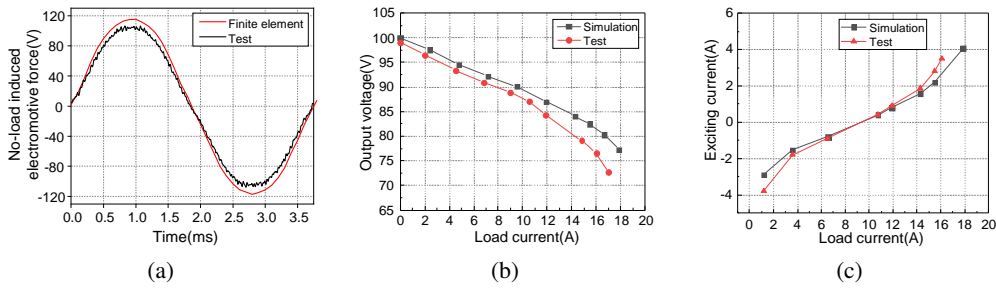


Fig. 17. Test waveform of the HESG: no-load induced electromotive force curve (a); external characteristic curve (b); field current regulation characteristic (c)

From Fig. 17(a), the HESG no-load induced electromotive force waveform and finite element analysis results are the same, the test waveform only has small distortion. There are fewer harmonics in the main magnetic field of HESG, and the prototype has a high output quality. From Fig. 17(b), when the HESG is operated at a fixed speed and exciting current condition, the output voltage decreases as the load current increases. Since the test uses a purely resistive load to simulate the starter generator load, the external characteristic curve of the HESG is obtained as almost a straight line. The output voltage of the test is slightly smaller than the finite element result, and the gap increases with the increase in load current, but the error of the two methods is small. When the rated load current is 11.9 A, the output voltage is 84.33 V, which meets the design requirement. From Fig. 17(c), the test and finite element results are basically, but when the load current is very large or small, there is a small error in the results of the two methods. When the load current increases from 3.57 A to 14.28 A, the curve is almost linear. The slope of the curve increases when the load current increases or decreases; at this time, increasing or decreasing load current requires a larger forward or reverse exciting current. When the load current is 16.07 A, the exciting current is 3.51 A, and the output power is 1 350 W, the HESG can realize a larger range of load current regulation and bear large loads.

6. Conclusions

Based on the operating point and demagnetization mechanism of PMs, this paper analyzes the operating process of PMs under different operating conditions of HESG and the influence of armature reaction magnetic field on the operating point and demagnetization of PMs, researches the operating point of average magnetic density and the rule of change of the smallest magnetic density value of the PMs under different loading conditions of the HESG, determines the position of demagnetization point of each PM and its influencing factors, and analyzes the influence law of the connecting magnetic isolation air gap parameter on the smallest magnetic density of two PM under consideration of the leakage and demagnetization of the end part of the PM. Moreover, analyse the influence law of the air gap parameters of TPMs and ICPMs on the minimum magnetic density of the two PMs, and preferably select the air gap parameters, and determine that the bottom angles of the left and right side of the air gap are 50° and 60° , respectively, and the height is 2 mm. At this

time, the minimum magnetic density of TPMs and ICPMs under a 50% overload condition of the generator is 0.47 T. The minimum magnetic density is 0.47 T and 0.45 T, which effectively ensures that the PMs are not demagnetised. Finally, a prototype test was carried out, and the results show that the HESG has a good no-load induced electromotive force curve and a wide range of magnetisation regulation, and it can also bear a large load under load conditions with good output performance.

References

- [1] Qin S.F., Xiong Y.Q., *Innovation strategies of Chinese new energy vehicle enterprises under the influence of non-financial policies: Effects, mechanisms and implications regulation*, Energy Policy, vol. 164, pp. 1–13 (2022), DOI: [10.1016/J.ENPOL.2022.112946](https://doi.org/10.1016/J.ENPOL.2022.112946).
- [2] Shannon N., *Preparing for the electric vehicle revolution*, Transmission & Distribution World, vol. 74, no. 5, pp. 56–57 (2022).
- [3] Guo J.Y., Yang J., Zhang Q.L., Wang J., Li F.Y., *Robust adaptive tracking control for range-extended electric vehicles*, 2020 39th Chinese Control Conference (CCC), Shenyang, China, pp. 5572–5576 (2020).
- [4] Li Y., Zhao C., Huang Y., Wang X., Guo F., Yang L., *Study on regenerative braking control strategy for extended range electric vehicles*, 2020 IEEE Vehicle Power and Propulsion Conference (VPPC), Gijon, Spain, pp. 1–6 (2020).
- [5] Cipek M., Kasac J., Pavkovic D., Zorc D., *A novel cascade approach to control variables optimisation for advanced series-parallel hybrid electric vehicle power-train*, Applied Energy, vol. 276, pp. 1–12 (2020), DOI: [10.1016/j.apenergy.2020.115488](https://doi.org/10.1016/j.apenergy.2020.115488).
- [6] Gu X.P., Zhang Z.R., Sun L.N., Yu L., *Magnetic field enhancement characteristic of an axially-parallel hybrid excitation DC generator*, IEEE Transactions on Magnetics, vol. 57, no. 2, pp. 1–5 (2020), DOI: [10.1109/tmag.2020.3012148](https://doi.org/10.1109/tmag.2020.3012148).
- [7] Hou J.I., Geng W.W., Li Q., Zhang Z.R., *3-D equivalent magnetic network modeling and FEA verification of a novel axial-flux hybrid-excitation in-wheel motor*, IEEE Transactions on Magnetics, vol. 57, no. 7, pp. 1–12 (2021), DOI: [10.1109/TMAG.2021.3081830](https://doi.org/10.1109/TMAG.2021.3081830).
- [8] Woo H.M., Lee D.H., *Characteristic analysis of parallel-rotor hybrid generator based on exciter types*, Journal of Power Electronics, vol. 20, no. 3, pp. 774–783 (2020), DOI: [10.1007/s43236-020-00068-w](https://doi.org/10.1007/s43236-020-00068-w).
- [9] Cui G., Xiong B., Huang K.J., Li Z.G., Ruan L., *Spatial distribution characteristics and influencing factors of demagnetization of permanent magnet motor for electric vehicle*, Transactions of China Electrotechnical Society (in Chinese), vol. 38, no. 22, pp. 5959–5974 (2023), DOI: [10.19595/j.cnki.1000-6753.tces.230533](https://doi.org/10.19595/j.cnki.1000-6753.tces.230533).
- [10] Xie Y., Jiang J.N., Cai W., Ren S.Q., Sun C.J., *Demagnetization failure of surface mount high speed permanent magnet synchronous motor and local infiltration of heavy rare earth*, Electric Machines and Control (in Chinese), vol. 28, no. 2, pp. 44–53 (2024), DOI: [10.15938/j.emc.2024.02.005](https://doi.org/10.15938/j.emc.2024.02.005).
- [11] Zhang D., Zhao J.W., Dong F., Song J.C., Dou S.K., Wang H., Xie F., *Partial demagnetization fault diagnosis research of permanent magnet synchronous motors based on the PNN algorithm*, Proceedings of the CSEE (in Chinese), vol. 39, no. 1, pp. 296–306+344 (2019), DOI: [10.13334/j.0258-8013.pcsee.172531](https://doi.org/10.13334/j.0258-8013.pcsee.172531).
- [12] Abbaszadeh K., Alam F.R., *On-load field component separation in surface-mounted permanent-magnet motors using an improved conformal mapping method*, IEEE Transactions on Magnetics, vol. 52, no. 2, pp. 1–12 (2016), DOI: [10.1109/tmag.2015.2493150](https://doi.org/10.1109/tmag.2015.2493150).
- [13] Baranski M., Szelag W., Lyskawinski W., *Analysis of the partial demagnetization process of magnets in a line start permanent magnet synchronous motor*, Energies, vol. 13, no. 21, pp. 1–20 (2020), DOI: [10.3390/en13215562](https://doi.org/10.3390/en13215562).

- [14] Jung J.W., Lee B.H., Kim K.S., Kim K.I., *Interior permanent magnet synchronous motor design for eddy current loss reduction in permanent magnets to prevent irreversible demagnetization*, *Energies*, vol. 13, no. 19, pp. 1–15 (2020), DOI: [10.3390/en13195082](https://doi.org/10.3390/en13195082).
- [15] Farshid Mahmouditabar, Abolfazl Vahedi, Nouredine Takorabet, *Design and analysis of interior permanent magnet motor for electric vehicle application considering irreversible demagnetization*, *IEEE Transactions on Industry Applications*, vol. 58, no. 1, pp. 284–293 (2022), DOI: [10.1109/ICEM49940.2020.9271060](https://doi.org/10.1109/ICEM49940.2020.9271060).
- [16] Wang X.G., Zhou C., Li X.H., Zhao M., Hu Z.X., *Research on rotor of hybrid permanent magnet synchronous motor for hybrid electric vehicle integrated starter generator*, *Electric Machines & Control Application (in Chinese)*, vol. 46, no. 5, pp. 107–112 (2019).
- [17] Sun Y.L., Liu Y., Lin W.Y., *The selection of magnet optimum operating point for EV's PMSM*, *Auto Electric Parts (in Chinese)*, no. 4, pp. 12–16 (2011).
- [18] Liu D., Tang Y.H., Liu L.S., *Calculation of permanent magnetic working points of polarity magnetic systems based on superposition*, *Marine Electric & Electronic Engineering (in Chinese)*, vol. 30, no. 2, pp. 45–49 (2010).
- [19] Wang Z.L., Cai W., *Study on electromagnetic demagnetization performance of rare earth interior permanent magnet synchronous motors*, *Micromotors (in Chinese)*, vol. 53, no. 3, pp. 15–19 (2020), DOI: [10.15934/j.cnki.micromotors.2020.03.004](https://doi.org/10.15934/j.cnki.micromotors.2020.03.004).
- [20] Chen Y.Y., Li Z.Y., Zhou X., Cai T.L., *Analysis and optimization of anti-demagnetization performance of composite structure hybrid permanent magnet motor*, *Electronic Measurement Technology (in Chinese)*, vol. 46, no. 11, pp. 1–6 (2023).
- [21] Xiao Y., Chen B., Li X., Shi J.F., Li Y., Wang D., *Simulation analysis of demagnetization for permanent magnet assisted Synchronous reluctance motors*, *Small & Special Electrical Machines (in Chinese)*, vol. 49, no. 7, pp. 9–13 (2021).
- [22] Yu F., Yao L., Chen S., *Demagnetization analysis and optimization design of interior permanent magnet synchronous motor*, *2020 23rd International Conference on Electrical Machines and Systems (ICEMS)*, Hamamatsu, Japan, pp. 704–709 (2020).
- [23] Liu K., Zeng C.B., Li M.X., Yang X.B., Zhou Y., *Fast equivalent magnetic circuit analysis of axial flux permanent magnet synchronous motor*, *Electronic Measurement Technology (in Chinese)*, vol. 46, no. 24, pp. 14–20 (2023).
- [24] Li B., Liang H.M., You J.X., Xiong F.Y., Jan K.S., *A non-linear permanent magnet working point migration model and its application to simulation of a polarized magnetic system*, *Journal of Magnetism*, vol. 24, no. 3, pp. 448–453 (2019), DOI: [10.4283/jmag.2019.24.3.448](https://doi.org/10.4283/jmag.2019.24.3.448).
- [25] Zhu J., Li S.H., Guo X.W., Nan H.C., Yang M., *Analytical calculation of leakage permeance of coreless axial flux permanent magnet generator*, *COMPEL - The International Journal for Computation and Mathematics in Electrical and Electronic Engineering*, vol. 41, no. 1, pp. 172–186 (2021), DOI: [10.1108/compel-04-2021-0140](https://doi.org/10.1108/compel-04-2021-0140).
- [26] Gao P., Gu Y.X., Shah S.H., Abubakar U., Wang X.Y., *Calculation and analysis of flux leakage coefficient of interior permanent magnet synchronous motors with fractional slot concentrated windings*, *IEEE Transactions on Applied Superconductivity*, vol. 29, no. 2, pp. 1–4 (2019), DOI: [10.1109/tasc.2019.2893740](https://doi.org/10.1109/tasc.2019.2893740).
- [27] Pen L., *Modeling and analysis of surface mounted permanent magnet synchronous motor with demagnetization fault*, MS Thesis (in Chinese), College of Electrical Engineering, Zhejiang University, Hangzhou (2024).

- [28] Xia P.P., Yu S.B., Dou R.T., *Analytical solution of magnetic field and study on the characteristics of surface mounted permanent magnet synchronous motor with asymmetrical magnetic poles*, Machine Tool & Hydraulics (in Chinese), vol. 52, no. 18, pp. 85–94 (2024).
- [29] Li X., Wang S.H., *Demagnetization analysis of the interior permanent magnet synchronous motor under different short circuit faults*, Journal of China Coal Society (in Chinese), vol. 42, no. S2, pp. 626–632 (2017).
- [30] Dantam R., Madhan B., *Selection of optimal magnets for traction motors to prevent demagnetization*, Machines, vol. 9, no. 6, pp. 124–124 (2021), DOI: [10.3390/machines9060124](https://doi.org/10.3390/machines9060124).
- [31] Wei M., *Research on demagnetization of permanent magnet of interior permanent magnet synchronous motor*, MS Thesis (in Chinese), School of Electrical Engineering, China University of Mining and Technology, Xuzhou (2023).
- [32] Zhang J.D., Shan W.T., Chen K.P., *Research and Optimization of Demagnetization Performance of PermanentMagnet Synchronous Motorized Spindle*, Machine Tool & Hydraulics (in Chinese), vol. 53, no. 1, pp. 24–31 (2025), DOI: [10.3969/j.issn.1001-3881.2025.01.004](https://doi.org/10.3969/j.issn.1001-3881.2025.01.004).
- [33] Alexander Kern, Nora Leuning, Kay Hameyer, *Semi-physical demagnetization model for the temperature dependency of permanent magnets in electrical machines*, AIP Advances, vol. 13, no. 2, 025105 (2023), DOI: [10.1063/9.0000400](https://doi.org/10.1063/9.0000400).
- [34] Zhu H., Xu Y., *Permanent magnet parameter design and performance analysis of bearing less flux switching permanent magnet motor*, IEEE Transactions on Industrial Electronics, vol. 68, no. 5, pp. 4153–4163 (2021), DOI: [10.1109/tie.2020.2984434](https://doi.org/10.1109/tie.2020.2984434).
- [35] You Y.M., Yoon K.Y., *Multi-objective optimization of permanent magnet synchronous motor for electric vehicle considering demagnetization*, Applied Sciences, vol. 11, no. 5, pp. 2159–2159 (2021), DOI: [10.3390/app11052159](https://doi.org/10.3390/app11052159).